Cross sections for OH transitions due to electron impact on water molecules

R. Scott Schappe and Erich Urban*
Department of Physics, Lake Forest College, Lake Forest, Illinois 60045, USA
(Received 27 February 2006; published 3 May 2006; publisher error corrected 5 May 2006)

We have measured absolute cross sections for electrons (9–700 eV) incident on water molecules. By fitting synthetic vibrational bands to the experimental emission spectra, we measured the emission cross sections for the OH $A\,^2\Sigma^+ - X\,^2\Pi$ (0,0), (0,1), (1,0), (1,1), (2,1), (2,2), (3,2), and (3,3) bands. The branching fractions from our cross sections are consistent with those we measured in the emission of a rf discharge and with our calculated transition rates. We have also calculated apparent level cross sections for the $A\,^2\Sigma^+ v'=0$, 1, 2, and 3 vibrational levels where the effects of predissociation are obvious.

DOI: 10.1103/PhysRevA.73.052702 PACS number(s): 34.80.Gs, 34.80.Ht

I. INTRODUCTION

The electron impact on water molecules is relevant in atmospheric, interstellar, technological, and biological systems. The dissociation and excitation of water by electrons is observed in the atmospheres of the earth and comets. Electron scattering from aqueous water molecules has been shown to behave similarly to gaseous H_2O [1]; ionizing radiation can create low-energy secondary electrons ($<$20 eV), which interact with water and can cause profound biological effects [2]. Furthermore, the OH A-X system is important as a diagnostic in combustion processes [3].

In the near ultraviolet (uv) through the infrared (ir), the $A\,^2\Sigma^+ - X\,^2\Pi$ system of OH produces the most intense emission from electron impact on water. Despite water's importance, there are significant inconsistencies in the cross-section studies for these emission bands. Previous work has focused primarily on the $(v'=0, v''=0)$ band, where v' and v'' denote the vibrational levels of the A and X states, respectively. Hayakawa first reported the relative energy dependence of this cross section [4]. Sushanin and Kisko [5] also measured the energy dependence of the OH A-X system and used a hydrogen Balmer cross section (from electron impact on water) of other researchers [6] to put their results for the (0,0) and (1,0) bands on an absolute scale. Tsurubuchi *et al.* [7] also measured these bands, using an unorthodox number density determination. Beenakker *et al.* [8] made a measurement of the absolute cross sections of the (0,0) band, as well as emission cross sections of the Balmer lines of hydrogen and the ir oxygen lines due to electron impact on H_2O.

The three previous absolute measurements of the (0,0) cross section for 40 eV electrons vary tremendously: Sushanin and Kisko report 3.4×10^{-19} cm^2, Beenakker *et al.* 66×10^{-19} cm^2, and Tsurubuchi *et al.* 400×10^{-19} cm^2. The cross-section energy dependence of Tsurubuchi *et al.* is also markedly different from those in other work. There is also the open question of whether these reported cross sections include the significant contributions from the other vibrational bands of the same system that overlap the reported bands.

In this experiment, we detect the uv radiation emitted from a quasistatic gaseous H_2O target penetrated by a beam of monoenergetic electrons to measure absolute emission cross sections. We report the individual cross sections for eight OH A-X bands—quadrupling the number of reported cross sections for this system. We have also calculated relative transition rates for the A-X system from molecular constants; our results are in agreement with previous calculations, other experimental measurements, and our experimental cross sections. These transition rates not only help us to check the consistency of our data, but also allow us to estimate the sizes of the cross sections of this system that are too small to detect directly in the electron beam experiment.

II. EXPERIMENT

A. Method

Monoenergetic electrons collide with and dissociate gaseous water molecules. Some of the OH fragments are in the $A\,^2\Sigma^+$ excited state and subsequently decay to the $X\,^2\Pi$ ground state, emitting light in the near uv. We measure the cross sections for this process using the optical method [9]. The absolute optical emission cross section $\sigma_{\mathrm{em}}(v',v'')$ is proportional to the fluorescence intensity emitted by the excited molecules. In addition, the cross section depends on the target density (n), electron flux (j), solid angle subtended by the collection optics (Ω), and optical efficiency (ε) of the detection system. The last we determine by replacing the electron beam signal with a lamp of known spectral irradiance. For the simplest case of unpolarized emission from a uniform density target

$$\sigma_{\mathrm{em}}(v',v'') = \frac{4\pi e}{\Omega \Delta x \Delta\lambda n I} S_{\mathrm{em}}(v',v''), \tag{1}$$

where I is the total electron beam current, Δx is the viewed length of the electron beam, $\Delta\lambda$ is the monochromator bandpass, and e is the magnitude of the electron charge. The absolute emission signal S_{em} (counts nm/s) is the experimental intensity I_{em} divided by the efficiency and then integrated over the vibrational band:

*Present address: Department of Physics, University of Wisconsin, Madison, WI 53706.

$$S_{\mathrm{em}}(v',v'') = \int \frac{I_{\mathrm{em}}(v',v'')}{\varepsilon} d\lambda. \quad (2)$$

Visually, S_{em} is the area under the band on the emission versus wavelength plot when the efficiency of the detection system is included.

In this experiment the gas is slowly flowed through the collision chamber, so the target density in the collision region density is not directly available. To determine the target number density we use a relative flow technique [9]. The target is formed by simultaneously flowing two gases where the partial pressure of each gas is known. The relation between the unknown OH cross section $\sigma_{\mathrm{OH}}(v',v'')$ and the known cross section for the calibration gas, σ_Y, is

$$\sigma_{\mathrm{OH}}(v',v'') = \sigma_Y \frac{S_{\mathrm{OH}}(v',v'')}{S_Y} \frac{p_Y}{p_{\mathrm{water}}}, \quad (3)$$

where Y is the species of the calibration gas, S is the relative integrated emission signal of the emission band (taking the efficiency into account) for the calibration gas or OH, and p_Y and p_{water} represent the respective partial pressures of the target gases.

Many of the OH emission cross sections are too small to detect directly in the electron beam experiment. We have two methods for determining these values: we can either use the experimental branching ratios derived from the discharge emission or, if these are not available, use the calculated transition rates.

Compared to a typical electron beam, the light emitted from a discharge is much more intense, and we use this increased intensity to help extract some of the weaker cross sections. Since the discharge does not possess a well-defined electron energy we cannot use Eq. (1) to determine the cross section. However, the cross sections are related to the emission signal and the transition rates:

$$\sigma(v',v_j'') \propto N_{v'} A(v',v_j'') \propto S_{\mathrm{em}}(v',v_j''), \quad (4)$$

where $N_{v'}$ is the population of the v' upper level, A is the transition rate, and S is the integrated emission signal in the discharge after accounting for the optical sensitivity. Taking the ratio of two different cross sections originating from the same parent v' level allows us to use a known electron beam cross section $\sigma(v',v_j'')$ to put an unknown cross section from the discharge, $\sigma(v',v_k'')$, on an absolute cross-section scale:

$$\sigma(v',v_k'') = \sigma(v',v_j'') \left(\frac{S_{\mathrm{em}}(v',v_k'')}{S_{\mathrm{em}}(v',v_j'')} \right)_{\mathrm{discharge}}. \quad (5)$$

We can also use Eq. (4) to provide a relationship between emission cross sections from the same parent level and the transition rates:

$$\sigma(v',v_j'') = \sigma(v',v_k'') \frac{A(v',v_j'')}{A(v',v_k'')}. \quad (6)$$

We use Eq. (6) to check the consistency of our experimental cross sections and calculated transition rates. Where experimental data are unavailable, we can use Eq. (6) to fill in these otherwise unmeasurable cross sections.

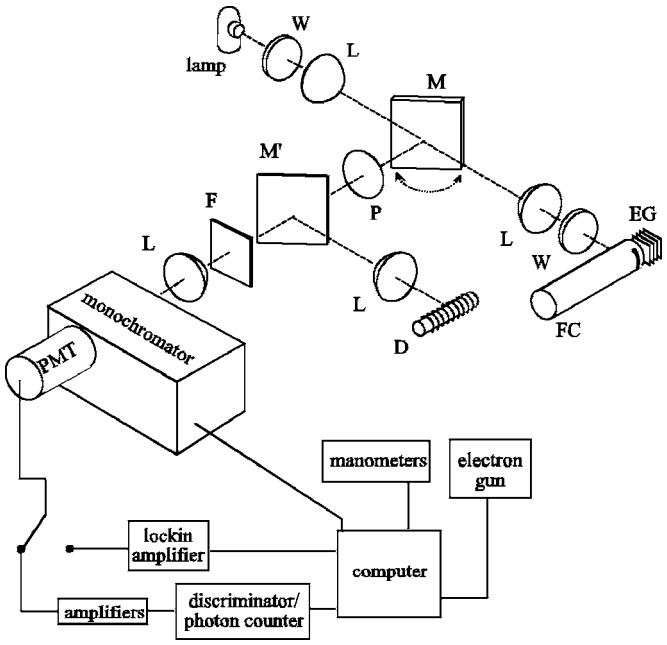

FIG. 1. An isometric representation of the apparatus. The electron gun (EG) emission is imaged by lenses (L) onto the entrance slit of the monochromator. The mirror (M) can be rotated to accept light from the calibration lamp or moved to position M′ to receive light from the rf discharge (D). The other symbols are explained in the text.

B. Apparatus

The apparatus we have used in this work has been more fully described elsewhere [10]. A schematic diagram of the apparatus is shown in Fig. 1. Briefly, the electron gun (labeled EG in Fig. 1) produces a beam with a typical energy spread of less than 1 eV and a total current of 15–140 μA at kinetic energies from 5 to 725 eV. A Faraday cup (FC) surrounds the electron beam and the total electron beam current is measured by an electrometer. The bottom of the Faraday cup can be biased to prevent secondary or scattered electrons from reentering the collision region. We found that the electron beam emission signal was linearly dependent on the electron beam current for 20 and 100 eV electrons. The vacuum system and electron gun are constructed from nonmagnetic stainless steel and the measured magnetic field within the collision chamber was 0.6 G (typical of the earth's magnetic field in this region) oriented perpendicular to the electron beam. Even near the OH onset energy (9.1 eV), the very slight curvature of the electron trajectories (R=17 cm) has a negligible effect upon the electron path length through the small observed volume of the collision region so we made no attempt to further reduce this field with external Helmholtz coils.

The radiation from the excited molecules exits the cup through a narrow slot in the side of the cup and emerges from the vacuum chamber through a fused silica viewport (W). A Corning BG24A filter (F) spectrally isolates the near-uv emission, which is imaged by lenses (L) onto the entrance slit of a $\frac{1}{4}$-m monochromator. A linear polarizer (P) can be added for polarization measurements. A cooled GaAs

(RCA C31034A-02) photomultiplier tube (PMT) detects the dispersed radiation and the PMT output pulses are amplified and sent to a photon counter and gate generator. The electron beam is modulated on and off with a period of 200 μs and a 50% duty cycle; photons are counted during an 88 μs gate while the electron beam is on (the *A* gate) and during another 88 μs gate while the electron beam is off (the *B* gate). The *B* gate contains the background counts (PMT dark counts, scattered light, etc.) and is subtracted from the *A* gate counts. We typically count for 50 000 gate pairs per data point. We determine the spectral response of the optical detection chain using a deuterium lamp with a known spectral irradiance (traceable to NIST). By rotating the plane mirror (M) the optical path for the lamp is identical to that of the radiation from the collision region.

The only significant difference from the system in Ref. [10] is that we flow the gas through the chamber in a quasistatic manner, rather than using a molecular beam. This prevents the buildup of contaminants due to the dissociated fragments, especially oxygen, which quickly degrade the cathode. Because the density in the chamber is not completely uniform—though it is constant over the small extent of the electron beam—we use Eq. (3) to put our results on an absolute scale. Our source of gaseous water is a reservoir containing about 50 ml of distilled, deionized liquid water, which we pump on repeatedly to remove any dissolved gases, and admit to the chamber through a leak valve. With a vapor pressure of about 18 Torr at room temperature, this makes for a very stable source.

We add nitrogen at a ratio of about 1:10 with the H_2O, measured by a capacitance manometer, in a reservoir upstream of the collision chamber. The gas enters the chamber via a 4.6 mm i.d. tube and the pressure in the chamber near the collision region is linearly dependent on the reservoir pressure—though with a slightly different proportionality constant for each species because of the different flow rates (water being about 25% faster than N_2). We also directly measure the pressures of the water and/or N_2 within the collision chamber with another capacitance manometer so that this disparity in the flow rates was not a factor in determining the relative target densities. The H_2O pressure in the collision chamber is in the range of 0.2–1.0 mTorr. We also found that the electron beam emission signal was linearly proportional to the gas partial pressures. The chamber walls are at or slightly above room temperature, and we observe no indications of any water condensation within the chamber.

We use the previously measured absolute emission cross sections for the (0,0) first negative band of N_2^+ at 391 nm [11] to put the OH cross sections on an absolute scale. The nitrogen emission bands that are in the region of the OH bands are from the triplet systems of N_2, which have cross sections that decrease very rapidly with increasing electron energy. By calibrating at 100 eV, the emission from these triplet systems is negligible, while the N_2^+ first negative band is at its maximum. To verify that the nitrogen calibration gas did not contaminate the OH emission bands we measured an initial spectrum for the water target alone, then added the nitrogen and recorded another spectrum. We did not observe any nitrogen features within or near the OH bands, and the absolute size of the OH bands was unaffected by the addition of the nitrogen.

To determine the characteristics of our electron beam we measure the relative cross section versus the electron energy of the aforementioned (0,0) band of the first negative system and the (0,0) band of the second positive system of N_2 at 337 nm [12,13]. The second positive system possesses a sharp peak just after a rapid onset, which makes it ideal for determining energy offset and energy spread of the electron beam. On the other hand, the excitation function of the first negative system has a broad maximum at 100 eV, so it is useful for checking the high-energy behavior of the electron gun. We found that our excitation functions for both of these systems were identical to the published results, confirming that the electron gun and Faraday cup were functioning properly.

To complement the electron beam measurements, we used a rf discharge source (D) also described in Ref. [10]. To measure discharge emission, the mirror (M) can be moved to position M′ using kinematic mounts. Because the rf noise from the source causes spurious photon counts, we use a lockin amplifier with a mechanical chopper to detect the PMT signal. The gaseous H_2O is slowly flowed through a quartz tube to prevent the buildup of contaminants. The steady-state pressure, measured by a capacitance manometer, is typically about 500 mTorr and during measurements it varies by less than 1%. The emission from the discharge is much more intense than from the electron beam, and the higher signal-to-noise ratio helps to bring out some of the weaker bands and the higher resolution that the discharge permits [0.40 nm full width at half maximum (FWHM)] reveals the heads of the weaker bands more clearly.

C. Analysis

1. Synthetic spectrum

The OH $A\ ^2\Sigma^+ - X\ ^2\Pi$ bands appear as sequences of overlapping bands: the most prominent is the $\Delta v = 0$ series starting at 306 nm. This peak is composed primarily of the (0,0) transition, but it also contains contributions from the (1,1),(2,2),… bands. Similarly, a smaller peak at 281 nm is the $\Delta v = 1$ series, comprised primarily of the (1,0) transition with progressively diminishing contributions from (2,1),(3,2),… . It is not obvious that previous researchers have separated these contributions, so we infer that their reported cross sections include all of the transitions of a given Δv progression.

To apportion the individual cross sections for these bands, we produced synthetic OH $A\ ^2\Sigma^+ - X\ ^2\Pi$ bands. From the standard quantum-mechanical theory, the emission intensity (in photons/s) for a rotational transition in a diatomic molecule can be expressed [14]

$$I \propto N_i S_{if} \nu^3 e^{-E_i/kT}, \tag{7}$$

where the *i* and *f* subscripts indicate the initial and final states, respectively, N_i is the population of the *i*th state, S_{if} is the rotational line strength, ν_{if} is the frequency of the transition, E_i is the rotational energy of the initial state, k is the Boltzmann constant, and T is the effective temperature.

Since the $A\ ^2\Sigma^+$ state has no orbital angular momentum along the internuclear axis, it conforms to Hund's case (b),

where the spin of the electron is coupled directly to the internuclear axis—as opposed to case (a) in which the spin is coupled first to the orbital angular momentum. The rotational energies of these states can be calculated from [15]

$$F_{1,2}(K') = B_{v'}K'(K'+1) - D_{v'}K'^2(K'+1)^2 \pm R_{v'}\left(K'+\tfrac{1}{2}\right), \tag{8}$$

where K' is the orbital angular momentum, $B_{v'}$ is the rotational constant, $D_{v'}$ accounts for the centrifugal distortion, and $R_{v'}$ describes the ρ-type doubling. The 1 and 2 superscripts refer to the total angular momentum J' cases $F_1(K')$, $J'=K'+\frac{1}{2}$, and $F_2(K')$, $J'=K'-\frac{1}{2}$.

On the other hand, the $X\,^2\Pi$ state is intermediate between the two Hund's coupling cases, so the energies of the doublet states are [15]

$$f_1(K'') = B_{v''}\left[(K''+1)^2 - 1 - \tfrac{1}{2}\sqrt{4(K''+1)^2 + a(a-4)}\right] - D_{v''}K''^2(K''+1)^2,$$

$$f_2(K'') = B_{v''}\left[K''^2 - 1 + \tfrac{1}{2}\sqrt{4K''^2 + a(a-4)}\right] - D_{v''}K''^2(K''+1)^2, \tag{9}$$

where $a=-7.547$ is the spin-orbit coupling constant and the 1 and 2 subscripts describe the equivalent relationship between K'' and J''. The values of B, D, and R were obtained from Ref. [15], and, as the subscripts imply, they depend on the parent vibrational state.

From the original work by Hill and Van Vleck [16], Earls [17] derived expressions for the line strengths of the O, P, Q, R, and S subbands of a $^2\Sigma^+$ to $^2\Pi$ system. Applying Eq. (7), (8), and (9) and the rotational line strength equations from Ref. [17], we produced a set of rotational transition lines for each vibrational transition. The rotational levels of the $A\,^2\Sigma^+$ state are increasingly predissociated with increasing v' primarily because of a crossing with the repulsive $^4\Sigma^-$ potential shown in Fig. 2. For the $v'=0$ level, predissociation is not significant until $N'=24$ while for $v'\geqslant 2$ all of the rotational levels experience significant depopulation via predissociation. We account for the diminished population, and thus the reduced emission intensity, for these higher rotational levels in our model by looking at the rate of change of the population of the ith rotational level, n_i:

$$\frac{dn_i}{dt} = P_i - n_i\left(\frac{1}{\tau_i} + \frac{1}{\tau_{\text{predis}}}\right), \tag{10}$$

where P_i represents the rate of populating the level (through electron collisions with H_2O), τ_i is the radiative lifetime [18], and τ_{predis} is the predissociation lifetime [19]. The population reaches steady state in the electron beam, so

$$n_i = P_i\left(\frac{\tau_{\text{predis}}\tau_i}{\tau_{\text{predis}} + \tau_i}\right). \tag{11}$$

In our model, the emission intensity is reduced by the factor in parentheses.

Each band has 12 branches (six primary and six satellite); from these hundreds of rotational transitions for each band, we construct the synthetic vibrational band by convoluting these rotational transitions with a 1.1 nm (FWHM) triangular bandpass, which reproduces the instrumental line profile of our monochromator. The overall intensity of each band is varied until we achieve an optimum fit for the sum of all synthetic bands to our experimental data.

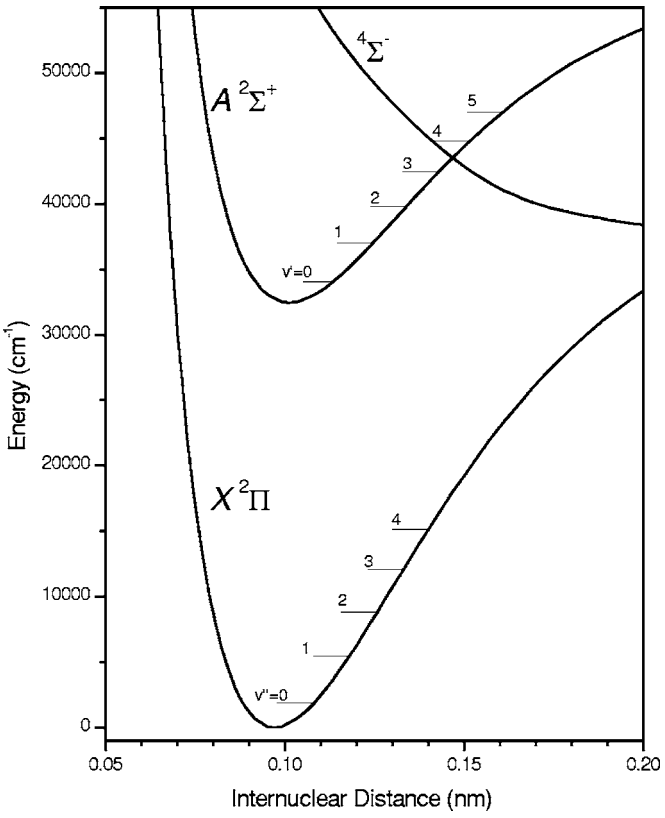

FIG. 2. The RKR potential curves for the $A\,^2\Sigma^+$ and $X\,^2\Pi$ states calculated from the molecular constants in Ref. [15]. Also shown is the repulsive $^4\Sigma^+$ state, which is largely responsible for the predissociation of some of the rotational levels of the $A\,^2\Sigma^+$ state.

Other than the band intensities, the only other free parameter for the fit is the effective temperature[1] for the rotational states in the OH molecules. It has been posited that two different dissociation pathways produce excited OH molecules: a singlet and a triplet channel [20–22]. From their emission spectra, Möhlmann *et al.* [20] suggest that these two channels produce different distributions of rotational-state populations and thus different effective temperatures. They propose a weighted distribution of four different temperatures ranging from 500 to 30 000 K, with the higher temperatures associated more with the higher rotational states. McConkey and co-workers have used LIF to measure the rotational population distributions of the $X\,^2\Pi\ v'=0$ level created by electron collisions with a supersonically cooled H_2O target [23]. Although their results show that decay from the A state is not a significant population mechanism for the X state, the X state, too, possess a rotational

[1]The electron dissociation and excitation processes do not produce OH fragments whose rotational level populations are in thermal equilibrium. Nevertheless, an effective temperature(s) can be determined for the purposes of emission spectra.

distribution not characterized by a single temperature. There has not been any LIF work to measure the relative rotational populations of the A state—at least in part due to the apparently small matrix elements connecting the $A\ ^2\Sigma^+\ v'=0$ level with levels of the higher-lying $B\ ^2\Sigma^+$ or $C\ ^2\Sigma^+$ states (see Sec. III).

We use a band that is a weighted average of three temperatures: 500, 4000, and 14 000 K. This produces a synthetic band that is an excellent match to our electron beam emission data. In selecting the weightings, we paid particular attention to the relative heights of the peaks, the slope of the red-degraded tail, and the abruptness of the rotational predissociation cutoff. The last of these is manifest as a change in slope at about 321 nm and again at 329 nm for the $\Delta v=0$ peak. For a given electron energy, the same weighting of the three temperatures was used for all bands. In general agreement with Möhlmann *et al.*, we found that the emission from higher electron energies was best fitted by a band with a larger weighting of the highest temperature.

Figure 3(a) shows our experimental emission spectrum for 19 eV incident electrons, adjusted for the optical sensitivity of our system. Below it in Fig. 3(b) is the synthetic spectrum fit and Fig. 3(c) shows the individual synthetic vibrational bands that comprise the fit. As Eq. (1) shows, the cross section for each transition is proportional to the area under the transition band. Using this fitting procedure, we were able to extract cross sections for several previously unmeasured vibrational bands. In addition to the dominant $(0,0)$ band at 306 nm, we were also able to extract cross sections for the $(1,1)$, $(2,2)$, and $(3,3)$ bands from the $\Delta v=0$ series. Similarly, for the $\Delta v=1$ series at 281 nm we extracted cross sections for the $(1,0)$, $(2,1)$, and $(3,2)$ transitions.

We applied a similar fitting procedure to our higher-resolution discharge data. Since the emission ratios from the same parent v' level of the A state are the same for the electron beam cross sections and the discharge, we used the discharge data as a consistency check on the ratios of our electron beam cross sections and indeed found good agreement: the branching fractions of the $v'=1$ and 2 levels agree to within 5%. We also used these discharge data along with Eq. (6) to determine the size of the $(0,1)$ band, which is not detectable above the noise in the electron beam data, but is just visible in the discharge spectrum.

Becker *et al.* [22] found that at 100 eV the polarization P for OH A-X system emission is negligible. Near threshold the polarization increases to a magnitude of about 7%; however, for some rotational transitions the polarization is positive and for others it is negative. Even if the emission were uniformly polarized, the polarization correction factor for Eq. (1) for observation at right angles to the electron beam would be $(1-P/3)^{-1}$, which would cause only a 2% correction to our peak cross section. Our measurements of the polarization for a large portion of the band at 100 and 19 eV showed no polarization within our experimental uncertainty, so a polarization correction is unnecessary.

2. Apparent emission cross sections

Table I shows our cross sections at 19 eV. The uncertainties for the bands are comprised of the uncertainties in the

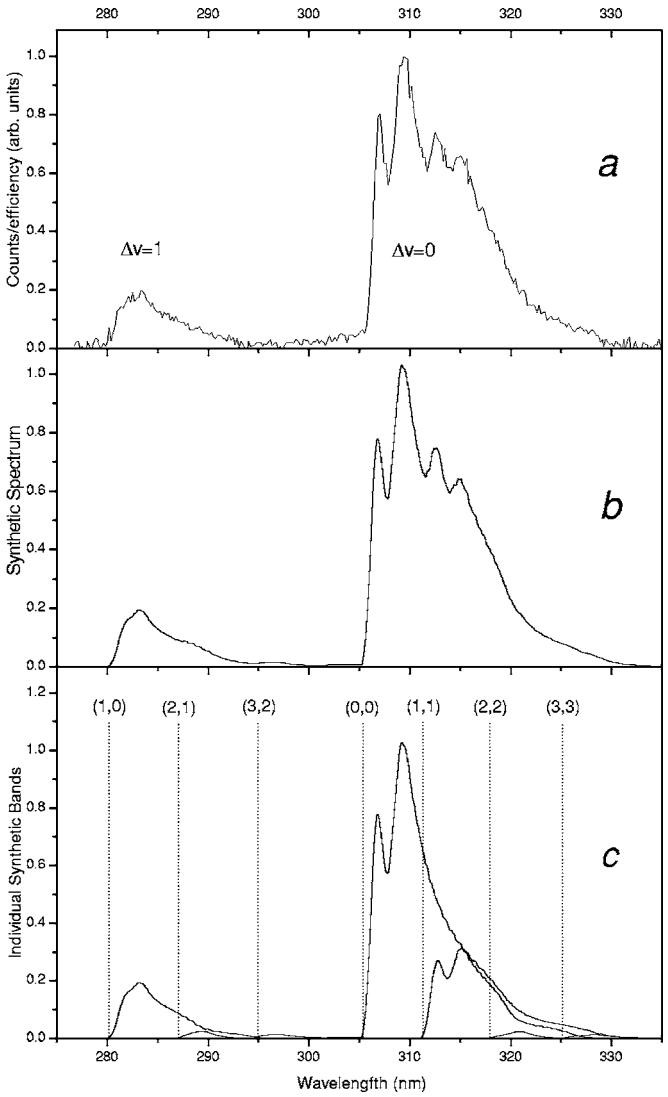

FIG. 3. (a) Our experimental data at 19 eV adjusted for the efficiency of the optical detection system. (b) The synthetic spectrum constructed from the molecular constants. (c) Individual bands that comprise the synthetic spectrum.

TABLE I. Absolute emission cross sections (units of $\times 10^{-19}$ cm^2) at 19 eV. The bold transition cross sections are used to scale the relative discharge emission or transition rates for a given v'. Cross sections in italics are from the transition rates; the $(0,1)$ cross section is from discharge data. The last column contains the apparent level cross sections for the vibrational levels of the A state. See text for information about the experimental uncertainties.

	X state (v'')					
A state (v')	0	1	2	3	4	Level
0	**76.6**	<0.49	*0.01*	*0.00*	*0.00*	77.1
1	12.0	**21.4**	*0.18*	*0.01*	*0.00*	33.6
2	*0.12*	**0.85**	<0.88	*0.01*	*0.00*	1.9
3	*0.02*	*0.25*	<**0.73**	<0.76	*0.00*	<1.8

TABLE II. Comparison of peak experimental emission cross sections (units of 10–19 cm^2).

Reference	(0, 0)	(1, 0)	Peak energy (eV)
This work	76.6	12.0	19
Ref. [8]	91		17
Ref. [5]	4.1	0.086	16
Ref. [7]	605	110	30
Ref. [21]			18

ratio of the pressures (2%), the stability of the electron beam (<0.5%), the irradiance of our calibrated lamp (5%), the measurement of the lamp emission (2%), the uncertainty of the N_2 reference cross section (10%), and of course the uncertainty in the integrated intensity of the emission band, S_{em}. The last varies depending on the size and distinctness of the band. The (0,0) band is the most reliable: S_{em} divided by beam current and pressure varies by less than 3% for separate data sets. Combining these uncertainties (in quadrature for independent errors) produces a total uncertainty for the (0,0) cross section of 15%, though the statistical variation at 19 eV absolute cross section is less than 6%. The (1,0) and (1,1) bands are also quite distinct, though because of their smaller size their total uncertainties are 20%. For the other bands, the total uncertainties are dominated by uncertainty in S_{em}: (2,1) band has uncertainties of 30% while the results for the (0,1), (2,2), (3,2), and (3,3) should be regarded as upper bounds.

Table II contains a comparison of the present results with previously reported values for the peak cross sections. The Tsurubuchi *et al.* [7] results are significantly larger than any other result; furthermore, they found that the (0,0) cross section reached its maximum at 30 eV, which is a much higher energy than all other results. They determined the target density by measuring the weight of a cooled thin metal pan inside the collision chamber. From the changing weight of the pan, they calculated the water condensation rate and thus inferred the target water density. It is possible that their unusual number density determination introduced some significant systematic error.

At the other extreme, Sushanin and Kisko's results [5] are much smaller than all others. They used the cross section of the hydrogen Balmer line ($n=4\rightarrow2$) at 486 nm from Ref. [6] to put their OH results on an absolute scale. Sushanin and Kisko do not describe how they account for the change in optical sensitivity from 486 nm to the OH bands at 306 and 281 nm. One of the known difficulties of using a tungsten lamp to calibrate uv wavelengths, however, is that the relatively meager uv output of the lamp is easily overwhelmed by scattering of the prodigious visible and ir radiation from the lamp into the optical system. This causes an overestimate of the uv optical sensitivity and results in uv cross sections that are too small.

The peak cross-section results of Beenakker *et al.* [8] for the OH (0,0) band are approximately 27% larger than our results. While these results agree when all uncertainties are included, if their reported cross section in fact includes the (1,1), (2,2), and (3,3) bands, then our results are very similar: our combined cross section for the $\Delta v=0$ peak is $(99\pm17)\times10^{-19}$ cm^2 compared with their value of $(91\pm15)\times10^{-19}$ cm^2.

3. Energy dependence

As mentioned earlier, other researchers have extensively explored the different dissociation pathways for H_2O: they found that the triplet dissociation path, which peaks just above threshold, is more likely to produce lower rotational states; at higher electron energies, higher rotational states are preferentially populated via the singlet path, which has a broad maximum at 40 eV [20]. Thus, at electron energies near threshold the lower rotational states are preferentially populated, making the emission near the bandhead more intense relative to the red-degraded tail; at higher energies the higher rotational states are favored, which causes the peaks near the bandhead to drop while enhancing the tail. Since the shape of the vibrational band changes as the electron energy increases, the determination of the energy dependence must include the entire band.

Because the energy dependence of the OH *A-X* emission varies according to the portion of the band observed, potentially the only reliable way to measure the energy dependence is to measure the relative cross sections for bands by applying the fitting procedure to the data at many different electron energies. We did this for the (0,0), (1,0), and (1,1) bands for 19, 40, 100, and 300 eV electrons. We found that, except for a slight shift of the onset, the overall energy dependence is not influenced by the upper vibrational level, which is consistent with the findings of the Ref. [21]. Since the general energy dependence of the cross sections is independent of the upper vibrational level, this suggests an easier alternative method: measuring the energy dependence for the *A-X* system by using the entire area of the $\Delta v=0$ or $\Delta v=1$ series. This method was in agreement with the fitting method described above for the 19, 40, 100, and 300 eV data.

Finally, to fill in other energies, we also measured the energy dependence by grossly decreasing the spectral resolution of the monochromator to 5 nm so that much of the $\Delta v=0$ peak was encompassed. Then we measured this signal divided by the beam current and chamber pressure as a function of the electron energy. This provides a mixture of low and high rotational quantum numbers and thus a balance of the triplet and single components. This technique was also consistent with the previous two methods. However, if we used the last method with a smaller bandpass (less than 2 nm FWHM), the energy dependence changed markedly as we sampled different wavelength intervals of the transition.

Figure 4 plots our relative energy dependence along with the other published work. The shape of our energy dependence curve is noticeably broader than most of the other curves. This may be due to our efforts to include the contributions from higher rotational states, which have a singlet-type energy dependence. Many of the previous researchers may have measured the energy dependence near the band's head, where lower rotational levels predominate.

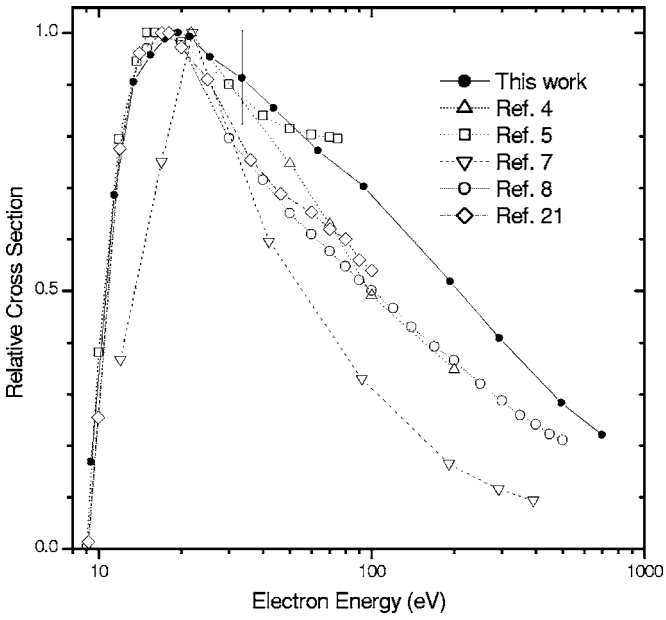

FIG. 4. The energy dependence of the cross section for the (0,0) band of the OH $A\,^2\Sigma^+ - X\,^2\Pi$ system. The curve of Ref. [7] has been shifted 8 eV to the left from their published data in order to put the onset nearer the accepted value.

4. Transition rates

Having a complete set of consistent transition rates for the system is useful for comparison with our measurements and for estimating the size of some cross sections. Several studies have been done previously, but for completeness we elected to recalculate our own set.

The combined efforts of Rydberg, Klein, and Rees (RKR) demonstrated that reliable diatomic potential energy curves can be derived from the vibrational and rotational energy level data [24]. Our RKR potentials for the $A\,^2\Sigma^+$ and $X\,^2\Pi$ states are derived from the molecular constants in Ref. [15] and calculated using software from Ref. [25]. From these calculated RKR potentials, which are shown in Fig. 2, we calculated the rotationless vibrational wave functions [26] for both states, for $v'=0$ through 3 and for $v''=0$ through 6.

For many molecules, the transition moment R_e varies slowly with internuclear distance. In this case the Franck-Condon principle applies and so the rate for vibrational transitions is proportional to $\nu^3 |\int \psi_{v'}^* \psi_{v''} dr|^2$, where ν is the frequency of the transition (the square of the overlap integral is also known as the Franck-Condon factor). For OH, however, the transition moment R_e changes significantly with internuclear distance [27], so we must include it in the integral for the transition rate:

$$A(v',v'') \propto \nu^3 \left| \int \psi_{v'}^* R_e \psi_{v''} dr \right|^2. \tag{12}$$

Table III shows our relative transition rates for the $v'=0-3$ vibrational levels of the A state decaying into the $v''=0-6$ levels of the X state. These are in good agreement with the calculations of Ref. [26], where they used an *ab initio* calculation using a Gaussian basis set to produce their wave functions. Our calculations are also in good agreement with the experimental transition rates [28,29].

TABLE III. Relative theoretical transition rates calculated from the RKR potentials.

	X state (v'')						
A state (v')	0	1	2	3	4	5	6
0	1000.0	4.1	0.1	0.0	0.0	0.0	0.0
1	322.8	603.7	5.0	0.4	0.0	0.0	0.0
2	65.3	477.1	321.9	3.6	1.3	0.1	0.0
3	11.7	167.0	486.5	143.6	1.4	3.1	0.4

Using Eq. (6), we compare the ratios of our experimental cross sections and calculated transition rates. For the (1,1) to (1,0) bands, our calculated transition rates are in a ratio of 1.9 while our experimental cross sections yield 1.8 ± 0.5. Theory predicts a value of 0.67 for (2,2):(2,1) branching fractions while our electron beam data yield 1.0 ± 0.3.

The theoretical ratio for the (0,0) to (0,1) transitions is 244, which is just outside the range for our experimental value 155 ± 70. The other potentially testable ratio, the (3,3):(3,2), contains too much uncertainty to be useful. Nevertheless, Eq. (6), the transition rates, and the measured cross sections are useful to estimate the cross sections that we could not observe in the electron beam or discharge data. As Table I shows, these cross sections are exceedingly small.

5. Level cross sections

As the name implies, a level cross section is the cross section for populating a vibrational level. The apparent level cross section is simply the sum of all of the emission cross sections originating from the level:

$$\sigma_{\text{app}}(v') = \sum_i \sigma(v', v_i''). \tag{13}$$

The resulting apparent level cross sections are included in Table I. We note that the contributions from the transitions inferred using Eq. (6) are nearly insignificant compared to the experimental cross sections and have very little effect on the level cross sections. We can also sum over all of the level cross sections to obtain the total cross section for excitation into the $A\,^2\Sigma^+$ state, which is 114×10^{-19} cm^2.

6. OH^+ system

The only other OH emission system in the same spectral region that might contaminate our measurements of the OH $A\,^2\Sigma^+ - X\,^2\Pi$ system is the $OH^+ A\,^3\Pi - X\,^3\Sigma^-$, which has been observed in discharges [30]. The region containing the (1,0), (0,0), and (1,1) bands of this system (at 333.2, 356.5, and 369.5 nm, respectively) is very empty, so the ion bands should be easy to observe. Despite the size of the cross section for OH^+ production [31], we saw no sign of these transitions at any incident electron energy in our electron beam spectra or in our discharge spectra. From this we estimate that the apparent emission cross sections for these transitions are less than 1×10^{-20} cm^2.

III. DISCUSSION

As Table I shows, the apparent level cross sections diminish rapidly with increasing v'. This is to be expected because the predissociation effects described in Sec. II C 1 become more significant for higher vibrational levels. The $v'=0$ level is largely unaffected, since only rotational levels above $N'=24$ show predissociation effects and at an effective temperatures on the order of 10^3 K these higher states are not significantly populated. On the other hand, the rotational levels of the $v'=1$ level show predissociation for $N'>14$, and this is reflected in the smaller apparent cross section for the $v'=1$ level. The effects of predissociation are even more severe for $v'=2$ and 3, in which all of the rotational levels are predissociated. The apparent level cross sections in the last column of Table I are based on the radiative emission alone and do not account for the $A\ ^2\Sigma^+$ molecules that are lost to dissociation; thus these values underestimate the actual cross section for electron excitation into the vibrational levels of the $A\ ^2\Sigma^+$ state.

Of interest for purposes of tracking energy deposition in water [32] or for the production rate of the OH dissociation products is the actual cross section for production of the $A\ ^2\Sigma^+$ state OH molecules. We can estimate these larger level cross sections for excitation into these predissociated vibrational levels by using the measured radiative lifetimes [18] and the predissociation lifetimes [19] and estimating the effective branching fractions for radiative versus radiative +dissociative losses. The radiative lifetimes are essentially the same for all of the rotational levels of a vibrational state and are nearly the same for the different v' levels, but as we described in Sec. II C 1, the predissociation lifetimes for the rotational levels associated with a given vibrational level decrease with increasing N'. To determine the effect of these dissociative losses on the system's emission intensities (and thus the cross sections), we again use our synthetic band calculations. We construct two bands for a given v': in addition to the bands that we created for fitting the spectrum [which include both radiation and predissociation using the factor from Eq. (11)], we also created bands that include only radiative transitions to the $X\ ^2\Pi$ state. The ratio of the nonpredissociated band to its predissociated counterpart gives us a quantitative guide to the effect of predissociation and a correction factor to apply to our apparent cross sections (the choice of $X\ ^2\Pi$ vibrational level does not affect this intensity ratio). For the $v'=0$ level, the predissociation losses are minimal and the factor is 1.05; so the cross section for excitation into the $v'=0$ level is only marginally larger: $(81\pm12)\times10^{-19}$ cm^2 at 19 eV. The $v'=1$ level is more predissociated and the intensity ratio of the nonpredissociated to predissociated band is 1.5, which produces a cross section of $(50\pm10)\times10^{-19}$ cm^2 at 19 eV. All of the rotational levels of the $v'=2$ level are significantly predissociated and now the ratio of the nonpredissociated to predissociated band leaps to 51. This yields a cross section of $(97\pm48)\times10^{-19}$ cm^2 at 19 eV and the lower bound seems consistent with the two previously calculated cross sections. The $v'=3$ level predissociation rates are about 1000 times faster than for the $v'=2$ level, which indicates that the $v'=3$ level cross section listed in Table I is a very conservative upper bound.

There are two weak OH systems that decay into the $A\ ^2\Sigma^+$ state: the $B\ ^2\Sigma^+-A\ ^2\Sigma^+$ in the visible and the $C\ ^2\Sigma^+-A\ ^2\Sigma^+$ in the near uv [33]. However, all of the observed transitions of these systems terminate on $A\ ^2\Sigma^+$ vibrational levels of $v'>3$, so they do not contribute to the populations of the $A\ ^2\Sigma^+$ levels that we are considering. Since there are no known cascade contributions to these A-state vibrational levels, the apparent level cross sections discussed above can, in fact, be considered direct level cross sections.

ACKNOWLEDGMENT

The authors wish to thank John Boffard for his helpful comments in the preparation of this manuscript.

[1] S. M. Pimblot, J. A. La Verne, and A. Mozunder, J. Phys. Chem. **100**, 8595 (1996).
[2] B. Boudaiffa, P. Cloutier, D. Hunting, M. A. Huels, and L. Sanche, Science **287**, 1658 (2000).
[3] J. O. Olsson, L. L. Andersson, M. Lenner, and M. Simonson, Rev. Sci. Instrum. **61**, 1029 (1990).
[4] G. Hayakawa, Proc. Phys. Math. Soc. Jpn. **26**, 78 (1944).
[5] I. V. Sushanin and S. M. Kisko, Opt. Spectrosc. **30**, 315 (1971).
[6] D. A. Vroom and F. J. De Heer, J. Chem. Phys. **50**, 1883 (1969).
[7] S. Tsurubuchi, T. Iwai, and T. Horie, J. Phys. Soc. Jpn. **36**, 537 (1974).
[8] C. I. M. Beenakker, F. J. De Heer, H. B. Krop, and G. R. Möhlmann, Chem. Phys. **6**, 445 (1974).
[9] A. R. Filippelli, C. C. Lin, L. W. Anderson, and J. W. McConkey, Adv. At., Mol., Opt. Phys. **33**, 1 (1994).
[10] R. S. Schappe, R. J. Edgell, and E. Urban, Phys. Rev. A **65**, 042701 (2002).
[11] W. L. Borst and E. C. Zipf, Phys. Rev. A **1**, 834 (1970).
[12] D. E. Shemansky, J. M. Ajello, and I. Kanik, Astrophys. J. **452**, 472 (1995).
[13] J. T. Fons, R. S. Schappe, and C. C. Lin, Phys. Rev. A **53**, 2239 (1996).
[14] G. Herzberg, *Molecular Spectra and Molecular Structure*, 2nd ed. (Krieger, Malabar, FL, 1989), Vol. I, Chaps. III and IV.
[15] G. H. Dieke and J. M. Crosswhite, J. Quant. Spectrosc. Radiat. Transf. **2**, 97 (1962).
[16] E. Hill and J. H. Van Vleck, Phys. Rev. **32**, 250 (1928).
[17] L. T. Earls, Phys. Rev. **48**, 423 (1935).
[18] K. German, J. Chem. Phys. **63**, 5252 (1975).
[19] G. Parlant and D. Yarkony, J. Chem. Phys. **110**, 363 (1999).
[20] G. R. Möhlmann, C. I. M. Beenakker, and F. J. De Heer, Chem. Phys. **13**, 375 (1976).
[21] K. Becker, B. Stumpf, and G. Schulz, Chem. Phys. Lett. **73**, 102 (1980).

[22] K. Becker, B. Stumpf, and G. Schulz, J. Phys. B **14**, L517 (1981).
[23] T. Harb, W. Kedzierski, and J. W. McConkey, J. Chem. Phys. **115**, 5507 (2001).
[24] A. L. G. Rees, Proc. Phys. Soc. London **59**, 998 (1947).
[25] R. J. Le Roy, University of Waterloo, Chemical Physics Research Report No. CP-657R, 2004 (unpublished).
[26] R. J. Le Roy, University of Waterloo, Chemical Physics Research Report No. CP-661, 2005 (unpublished).
[27] C. W. Bauschlicher and S. R. Langhoff, J. Chem. Phys. **87**, 4665 (1987).
[28] R. A. Copeland, J. B. Jeffries, and D. R. Crosley, Chem. Phys. Lett. **138**, 425 (1987).
[29] K. L. Steffens, J. Luque, J. B. Jeffries, and D. R. Crosley, J. Chem. Phys. **106**, 6262 (1997).
[30] F. W. Loomis and W. H. Brandt, Phys. Rev. **49**, 55 (1935).
[31] J. Schutten, F. J. De Heer, H. R. Moustafa, A. J. H. Boerboom, and J. Kristemaker, J. Chem. Phys. **44**, 3924 (1966).
[32] J. J. Olivero, R. W. Stagat, and A. E. S. Green, J. Geophys. Res. **77**, 4797 (1972).
[33] R. W. B. Pearse and A. G. Gaydon, *The Identification of Molecular Spectra*, 4th ed. (Chapman and Hall, London, 1976), pp. 264–265.